

# Plastic behavior of fcc metals over a wide range of strain: Macroscopic and microscopic descriptions and their relationship

Tamás Csanádi<sup>a</sup>, Nguyen Q. Chinh<sup>a,\*</sup>, Jenő Gubicza<sup>a</sup>, Terence G. Langdon<sup>b,c</sup>

<sup>a</sup> Department of Materials Physics, Eötvös University Budapest, H-1117 Budapest, Pázmány P. sétány 1/A., Hungary

<sup>b</sup> Departments of Aerospace & Mechanical Engineering and Materials Science, University of Southern California, Los Angeles, CA 90089-1453, USA

<sup>c</sup> Materials Research Group, School of Engineering Sciences, University of Southampton, Southampton SO17 1BJ, UK

Received 1 November 2010; received in revised form 16 December 2010; accepted 17 December 2010

Available online 20 January 2011

## Abstract

The room temperature macroscopic and microscopic plastic behavior of four face-centered cubic metals (Al, Au, Cu and Ni) is investigated experimentally over a wide strain range, and theoretical modeling is used to simulate the established major micromechanisms describing the evolution of mobile and forest dislocations during plastic flow. It is shown that forest dislocations develop primarily due to interaction between mobile dislocations, while the contribution from forest–mobile interactions is only minor. The trapping of mobile dislocations and the annihilation of forest dislocations are both controlled by the same thermally activated dislocation motion. These observations permit a simplification of the theoretical model that leads to an analytical relationship for the evolution of the total dislocation density as a function of strain. From this analysis, correlations are drawn between the macroscopic parameters describing the stress–strain relationship and the fundamental characteristics of the microscopic processes.

© 2010 Acta Materialia Inc. Published by Elsevier Ltd. All rights reserved.

**Keywords:** fcc Metals; Severe plastic deformation (SPD); Thermally activated processes; Stress–strain relationship; Dislocation density

## 1. Introduction

The plastic deformation of face-centered cubic (fcc) metals has been extensively investigated for many years. Detailed descriptions have been developed to explain the basic deformation processes operating in the early stages, designated as I, II and III in single crystals [1–4]. Two additional stages, denoted as IV and V, become evident at large strains for polycrystalline metallic materials [5,6]. The description of the macroscopic stress–strain behavior and a deep understanding of the role of the underlying microscopic mechanisms are important from the viewpoint of both materials science and engineering applications. Although the basic microscopic processes of plastic deformation are well known in metallic materials, the correlation between the characteristics of these processes and the

parameters describing the macroscopic mechanical behavior is not fully understood. An identification of the main deformation mechanisms determining the mechanical properties at high strains is also of great importance since severe plastic deformation (SPD) procedures are the favored methods for producing bulk ultrafine-grained (UFG) metals [7–9]. One of the most useful SPD procedures is equal-channel angular pressing (ECAP) [10,11] which can produce relatively homogeneous UFG microstructures in bulk samples. Therefore, processing by ECAP may be used to prepare specimens for an investigation of plasticity to very high strains.

Although there are numerous models for both the phenomenological and the microscopic descriptions of plastic deformation, a uniform description is not yet available. The various descriptions of the microscopic processes differ primarily in terms of their treatment of the dislocations. There are models considering the effect of the total dislocation densities [12–15] and other models dealing with mobile

\* Corresponding author. Tel.: +36 1 3722845.

E-mail address: [chinh@metal.elte.hu](mailto:chinh@metal.elte.hu) (N.Q. Chinh).

and forest dislocations [16]. There are also descriptions where the dislocations are separated according to their appearance in the cell interiors or cell walls formed in the deformed microstructures [17,18]. All of these macroscopic and microscopic models are generally in good agreement with the experimental results despite their different approaches. However, it is reasonable to assume that these models are based on the same underlying physical principles, and therefore should be interconnected.

The background of the present analytical treatment is to examine the relationship between a recent macroscopic description [19,20] and the microscopic processes adopted in the classic Kubin–Estrin (KE) model [16]. Thus, this work can be regarded as a continuation of the most recent report [20] where the room temperature plastic behavior of pure Al, Ni, Cu and Au was studied over a wide range of strain and then related to the melting points of the different metals. The earlier results revealed that the saturation flow stress and the maximum dislocation density may be scaled with the absolute melting point of the material. In the present analysis it is shown that the microscopic KE model, which describes separately the evolution of mobile and forest dislocations, can be simplified to give a closed-form solution for the total dislocation density as a function of strain. Furthermore, the relationships between the parameters characterizing the microscopic processes and the quantities of the phenomenological description are deduced and examined.

## 2. Background to the analysis

### 2.1. Macroscopic description: true stress–true strain relationships

Analyzing the homogenous plastic deformation of several fcc metals deformed at room temperature (RT), it was shown earlier that the macroscopic stress–strain ( $\sigma - \varepsilon$ ) relationship may be fitted by a constitutive relationship of the form [19,20]:

$$\sigma = \sigma_o + \sigma_1 \left\{ 1 - \exp \left[ - \left( \frac{\varepsilon}{\varepsilon_c} \right)^n \right] \right\}, \quad (1)$$

where  $\sigma_o$ ,  $\sigma_1$ ,  $\varepsilon_c$  and the exponent  $n$  are fitting parameters and the strain  $\varepsilon$  is taken as the absolute amount of strain relative to the initial state. Physically, the first constant,  $\sigma_o$ , is the friction stress related to the onset of plastic deformation which is then described by the three fitting parameters,  $\sigma_1$ ,  $\varepsilon_c$  and  $n$ . The relevant values of these parameters

Table 1  
The parameters of the constitutive Eq. (1) obtained by fitting the stress–strain data for different fcc metals.

Metal	$\sigma_o$ (MPa)	$\sigma_1$ (MPa)	$\varepsilon_c$	$n$
Al	21	101	0.79	0.69
Au	24	219	0.27	0.72
Cu	49	322	0.17	0.86
Ni	86	1013	0.39	0.76

for some fcc metals are given in Table 1. It is important to emphasize, as noted earlier [19,20], that Eq. (1) incorporates the well-known Hollomon [21] and Voce-type [22] equations. Taking  $n = 1$ , Eq. (1) leads to the Voce-type exponential equation:

$$\sigma = \sigma_o + \sigma_1 \left[ 1 - \exp \left( - \frac{\varepsilon}{\varepsilon_c} \right) \right], \quad (2)$$

or the original Voce equation:

$$\frac{\sigma_{sat} - \sigma}{\sigma_{sat} - \sigma_o} = \exp \left( - \frac{\varepsilon}{\varepsilon_c} \right), \quad (3)$$

where the saturation stress is given as:

$$\sigma_{sat} = \sigma_o + \sigma_1. \quad (4)$$

Furthermore, expressing Eq. (1) as a Taylor expansion at small strains leads to:

$$\sigma = \sigma_o + K \cdot \varepsilon^n, \quad (5)$$

which is the conventional power-law Hollomon relationship where  $K$  is a constant.

Recently it was shown that the saturation stress,  $\sigma_{sat}$ , obtained at RT for different fcc metals can be scaled by the absolute melting point,  $T_m$  [20], thereby suggesting that microstructural saturation is determined by thermally activated deformation mechanisms. Furthermore, the deformation process in the saturation state may be regarded as a steady-state flow, leading to a uniform description of the plastic behavior of the highly deformed bulk fcc metals. Considering the effect of microscopic mechanisms, it was shown also that dislocation-based processes determine the saturation strength. The following section summarizes the effects of these basic processes on the plastic behavior of fcc metals.

### 2.2. Microscopic description: the effect of dislocation-based mechanisms

The evolution of the dislocation density during plastic deformation is affected by the formation and annihilation processes as well as by the interaction between dislocations. The dislocation reactions may result in their trapping and therefore two types of dislocation densities may be identified:  $\rho_m$  for mobile dislocations and  $\rho_f$  for forest dislocations. The average total dislocation density,  $\rho$ , is then the sum of these two component parts so that  $\rho = \rho_m + \rho_f$ . Earlier studies [19,20] showed that the KE model [16] can be effectively used to describe the development of these dislocation densities. In this model, the approach requires a numerical solution of the following equations for pure metals:

$$\frac{d\rho_m}{d\varepsilon} = C_1 - C_2 \cdot \rho_m - C_3 \cdot \rho_f^{1/2}, \quad (6a)$$

and

$$\frac{d\rho_f}{d\varepsilon} = C_2 \cdot \rho_m + C_3 \cdot \rho_f^{1/2} - C_4 \cdot \rho_f, \quad (6b)$$

where the terms containing the parameters  $C_i$  are related to the primary competing microscopic processes occurring during plastic deformation such as the multiplication of mobile dislocations ( $C_1$ ), their mutual trapping ( $C_2$ ), their immobilization through interactions with forest dislocations ( $C_3$ ) and the advent of dynamic recovery ( $C_4$ ).

The values of the parameters  $C_i$  for different pure fcc materials were determined by applying Eqs. (6a) and (6b) so that their numerical solution describes best the experimental dislocation density as a function of strain deduced from tensile stress–strain data obtained on annealed samples [19,20]. The relevant values of the parameters  $C_i$  for Al, Ni, Cu and Au are listed in Table 2. The use of these values then permits a direct comparison between the roles of individual micromechanisms operating during plastic deformation of different fcc metals. It is important to emphasize that for all fcc metals investigated here, the value of  $C_3\rho_f^{1/2}$  is at least one order of magnitude smaller than any of the other terms in Eqs. (6a) or (6b) over the entire strain regime, where this is demonstrated directly in Fig. 1 for Al. This means that during the plastic deformation of fcc metals at room temperature the reduction in the mobile dislocation density can be essentially attributed to the trapping mechanism related to the interaction between mobile dislocations (characterized by the term  $C_2\rho_m$ ), rather than to the effect of forest dislocations. The results of the numerical calculations based on Eqs. (6a) and (6b) also show that the values of  $C_2$  and  $C_4$  are practically the same for all metals.

It should be noted that during the fitting procedure the best values of the parameters  $C_i$  were chosen so that the usual mathematical variance characterizing the usability of the fitting procedure is minimal. Results of the sensitivity analysis show that when the value of the minimal variance is changing within 1%, the values of  $C_2$  and  $C_4$  remain almost the same. A relative difference higher than 20% between these two parameters will lead to a drastic increase in the variance, confirming that the coincidence of the coefficients  $C_2$  and  $C_4$  is genuine.

Neglecting the term containing parameter  $C_3$  and noting the equality of  $C_2$  and  $C_4$ , it is possible to draw important conclusions concerning the plastic behavior of fcc metals that significantly extend the implications of the earlier report [20]. Thus, this paper presents these additional macroscopic and microscopic features of plasticity and discusses their relationships for fcc metals.

Table 2

The values of  $C_i$  parameters in Eqs. (6a) and (6b) determined by simulations of the experimental stress–strain curves for the four fcc metals. (These parameters were reported in Ref. [20], where the real value of  $C_2$  and  $C_4$  was—unfortunately by mistake—multiplied by a factor of 1.87)

Metal	$C_1$ (1/m <sup>2</sup> )	$C_2$	$C_3$ (1/m)	$C_4$
Al	$1.87 \times 10^{14}$	1.0	$9 \times 10^5$	1.2
Au	$3.91 \times 10^{15}$	3.1	$2 \times 10^6$	3.6
Cu	$7.23 \times 10^{15}$	5.6	$3 \times 10^6$	5.9
Ni	$8.32 \times 10^{15}$	2.5	$4 \times 10^6$	2.6

### 3. Additional macroscopic and microscopic behaviors of plastic deformation in fcc metals

#### 3.1. Ratio of the mobile and forest dislocation densities in the saturation state

As already noted, the results of the evaluation of the experimental data using Eqs. (6a) and (6b) show that the term  $C_3\rho_f^{1/2}$  may be neglected over the total deformation region for all fcc metals studied here. Therefore, Eqs. (6a) and (6b) are simplified as:

$$\frac{d\rho_m}{d\varepsilon} = C_1 - C_2\rho_m, \tag{7a}$$

and

$$\frac{d\rho_f}{d\varepsilon} = C_2\rho_m - C_4\rho_f, \tag{7b}$$

respectively. In the saturation state, the latter equation leads to the relationship:

$$C_2\rho_{m,sat} - C_4\rho_{f,sat} = 0, \tag{8}$$

so that:

$$\frac{\rho_{m,sat}}{\rho_{f,sat}} = \frac{C_4}{C_2}, \tag{9}$$

where  $\rho_{m,sat}$  and  $\rho_{f,sat}$  are the saturation mobile and forest dislocation densities, respectively. The similarities in values of  $C_2$  and  $C_4$  (Table 2) results in similar saturation densities for the forest and mobile dislocations. These similar values of  $C_2$  and  $C_4$  also suggest that both the formation and annihilation of forest dislocations are based on the same mechanism and this may be explained by the following simple model of dislocation interaction.

When a mobile dislocation is intersected by another dislocation gliding on a non-coplanar plane, a jog and/or a kink is formed. A kink lies in the slip plane and does not impede the motion of the dislocation but a jog lies out of the original slip plane and may hinder further dislocation glide. Fig. 2 shows schematically a jog on a dislocation

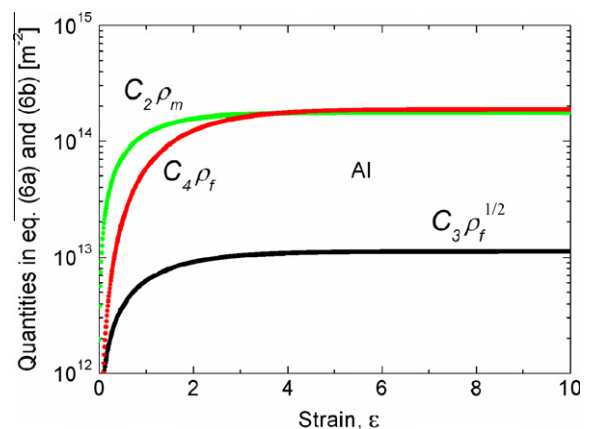


Fig. 1. The quantities of  $C_2\rho_m$ ,  $C_4\rho_f$  and  $C_3\rho_f^{1/2}$  numerically calculated for Al as a function of strain, demonstrating their contributions in Eqs. (6a) and (6b).

denoted by  $A$  having an original glide plane  $S_1$ ; a segment of this dislocation has moved to plane  $S_2$  due to the intersection with the other dislocation. The direction and the length of the jog correspond to the Burgers vector ( $b_2$ ) of the other dislocation. A similar jog or a kink may be formed on the other dislocation but its direction and length correspond to the Burgers vector ( $b_1$ ) of dislocation  $A$ . If more than one dislocation intersects dislocation  $A$  at the same location, the length of the jog is increased.

The two segments of dislocation  $A$  in planes  $S_1$  and  $S_2$  are gliding due to the resolved shear stress in the directions indicated by the arrows in Fig. 2. Usually the slip plane of the jog does not lie in the moving direction of the gliding segments in planes  $S_1$  and  $S_2$  and therefore the jog can follow these segments only by a non-conservative motion. Due to the difficulty of this motion at RT, the jog is rather immobile or falls behind the gliding segments, and as a result, the two gliding segments bow out in planes  $S_1$  and  $S_2$ . The successive stages of dislocation motion are marked by superscript roman numbers in Fig. 2. During this motion, the sections close to the jog become more parallel to each other: these segments are denoted by thick solid and dashed lines in Fig. 2 and they have opposite signs so that there is an attractive interaction between them. If the original dislocation is edge or screw type, these segments have screw or edge character and therefore they can move towards each other by cross-slip or climb, respectively. The faster the cross-slip or climb of these segments, the higher the probability of the formation of an immobile dipole in trapping. These dipoles constitute the forest dislocations, and both their formation and annihilation are controlled by the same thermally activated processes (cross-slip or climb) which explains the close values of  $C_2$  and  $C_4$  for each fcc metal. The parameter  $C_2$  characterizing the probability of forest formation is larger if the rate of dislocation multiplication is higher ( $C_1$ ) because the chance of forming new jogs then increases; cross-slip and climb are also easier. For example, for a higher homologous temperature where RT corresponds to a homologous temperature of  $293/T_m$ , the ratios  $C_2/C_1$  and  $C_4/C_1$  increase with decreasing melting point as was shown previously (Fig. 5 in Ref. [20]).

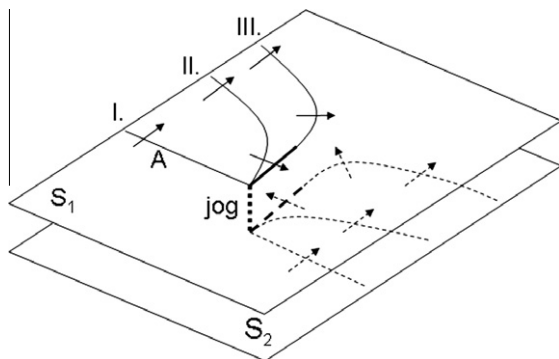


Fig. 2. A schematic figure illustrating the motion of a mobile dislocation at a jog formed due to the intersection of another mobile dislocation. See text for details.

It is noted that cross-slip occurs more easily than climb at RT due to the smaller activation energy of the former process; the trapping and annihilation of screw dipoles is therefore much faster than for edge dipoles. Moreover, when the plane containing the  $b_1$  and  $b_2$  vectors is an easy glide plane, the jog formed on an edge dislocation can follow the gliding segments in planes  $S_1$  and  $S_2$ , and in this case screw dipoles are not formed at the jog. As a result, the character of the dislocation structure is usually shifted to an edge type with increasing strain as was shown in previous reports [23,24]. The trapping and annihilation of edge dipoles by climb is controlled by vacancy diffusion and this process is not very fast in coarse-grained metals at RT. At the same time, the segments in the dipoles are very close to each other, with a spacing of about several Burgers vectors, and therefore the attractive forces between them are very large and this effectively assists the climb process. Furthermore, it was also shown [25] that with increasing strain the vacancy diffusion becomes much faster due to the very high concentration of deformation-induced excess vacancies [26] and their easier migration along dislocations and grain boundaries. As a result, the trapping and annihilation of edge forest dipoles during deformation may be significant even at RT.

This simple model also explains the lack of significance of any interaction between the mobile and forest dislocations in the decrease of mobile and the increase of forest dislocation densities. If a mobile dislocation intersects a forest dipole, two parallel jogs develop on the mobile dislocation as shown in Fig. 3. The direction and the length of the jogs correspond to the Burgers vector ( $b_1$ ) of the dislocations in the forest dipole. The distance between the jogs,  $d$ , is basically determined by the spacing between the dislocations in the dipole. The segments outside the jog-pair can slip further on plane  $S_3$ . The glide plane of the segment between the two jogs is plane  $S_4$  and the length of this segment,  $d$ , is small since the distance between the dislocations in a forest dipole is very small. As a consequence, the glide of the segment in plane  $S_4$  needs a much higher stress than for the dislocation segments in plane  $S_3$  and therefore in practice the former dislocation remains immobile.

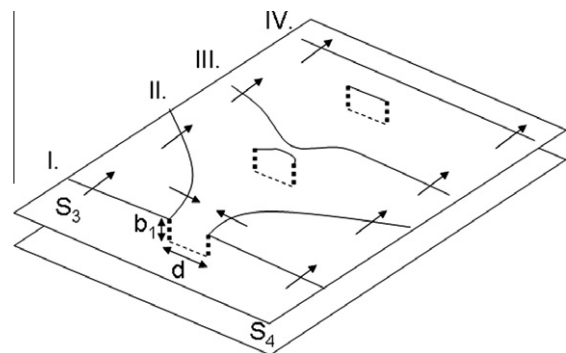


Fig. 3. A schematic figure illustrating the motion of a mobile dislocation at a jog-pair formed after the intersection of a forest dipole. See text for details.

The successive stages of dislocation motion are marked by superscript roman numbers in Fig. 3. The two dislocation segments in plane  $S_3$  bow out due to the resolved stresses, leading to two segments close to the jogs and having opposite sign. Later, they are annihilated and a mobile dislocation glides further while a loop is left behind. As  $b_1$  and  $d$  are small, this loop can annihilate easily by cross-slip or climb. Consequently, when a mobile dislocation intersects a forest dipole, the mobile and forest densities change only slightly, which explains the much smaller value of  $C_3\rho_f^{1/2}$  compared to the other terms in Eqs. (6a) or (6b).

### 3.2. Description of dislocation density evolution by using the simplified KE model

Considering Eqs. (7a) and (7b) of the simplified KE model and using the total dislocation density  $\rho = \rho_m + \rho_f$ , leads to:

$$\frac{d\rho}{d\varepsilon} = C_1 - C_4\rho_f. \quad (10)$$

Differentiating this equation with respect to  $\varepsilon$  leads to:

$$\frac{d^2\rho}{d\varepsilon^2} = -C_4\frac{d\rho_f}{d\varepsilon} = -C_4(C_2\rho_m - C_4\rho_f). \quad (11)$$

Substituting  $\rho_m = \rho - \rho_f$  and  $C_4\rho_f = C_1 - \frac{d\rho}{d\varepsilon}$  into Eq. (11) and rearranging gives the second-order differential equation for the total dislocation density,  $\rho$ :

$$\frac{d^2\rho}{d\varepsilon^2} + (C_2 + C_4)\frac{d\rho}{d\varepsilon} + C_2C_4\rho - C_1(C_2 + C_4) = 0. \quad (12)$$

It is apparent that the role of parameters  $C_2$  and  $C_4$  is symmetrical in Eq. (12). According to the results of numerical simulation, it is reasonable to take the parameters  $C_2$  and  $C_4$  as equal. For this condition, Eq. (12) can be expressed in the form:

$$\frac{d^2\rho}{d\varepsilon^2} + 2C_4\frac{d\rho}{d\varepsilon} + C_4^2\rho - 2C_1C_4 = 0, \quad (13)$$

which has a closed-form analytical solution given by:

$$\rho(\varepsilon) = \frac{2C_1}{C_4} - \left(\frac{2C_1}{C_4} - \rho_0\right) \left(1 + \frac{C_4\varepsilon}{2}\right) \exp(-C_4\varepsilon), \quad (14)$$

where  $\rho_0$  is the initial dislocation density at  $\varepsilon = 0$  ( $\rho(0) = \rho_0$ ). This is taken as  $6 \times 10^{11}$ ,  $1 \times 10^{13}$ ,  $3 \times 10^{13}$  and  $3 \times 10^{13} \text{ m}^{-2}$  for Al, Au, Cu and Ni, respectively, for the best solutions in the present analysis. In the solution of Eq. (13) the initial value of the first derivative of  $\rho$  is given by Eq. (10) as  $\rho'(0) = C_1 - C_4\rho_f(0)$  and as a first approximation, it is reasonable to take  $\rho_m(0) = \rho_f(0) = \frac{\rho(0)}{2} = \frac{\rho_0}{2}$  in every calculation. Using Eqs. (7a) and (7b) of the simplified KE model and taking  $C_4 = C_2$ , the values of the parameters  $C_1$  and  $C_4$  are determined from the experimental stress–strain data in the same way as described in Section 2.2. The values of parameters  $C_1$  and  $C_4$  determined by the simplified KE model are listed in Table 3. It can be seen that they are only slightly different from the values obtained using the original KE model as

Table 3

The values of parameters  $C_1$  and  $C_4$  determined by Eq. (13) of the simplified KE model.

Metal	$C_1$ (1/m <sup>2</sup> )	$C_4$
Al	$1.87 \times 10^{14}$	1.09
Au	$3.89 \times 10^{15}$	3.28
Cu	$7.21 \times 10^{15}$	5.98
Ni	$8.27 \times 10^{15}$	2.52

given in Table 2. Fig. 4a plots, for example, the best solutions of Eqs. (6a), (6b), and (13) for Al and the corresponding numerically calculated stress–strain curves are shown in Fig. 4b together with the experimental data obtained at room temperature. It can be seen that both numerical solutions agree well with the experimental data over a wide range of strain. Similar excellent correlations were also obtained for the other four fcc metals, thereby providing support and confirmation for the validity of the modified Eq. (13) of the KE model.

Considering Eq. (13) for the total dislocation density and its analytical solution given in Eq. (14), it is anticipated that the KE model can be compared with others describing the development of the total dislocation density, and the effect of different micromechanisms may be related to the characteristics of the macroscopic descriptions. In the following section, some applications of Eqs. (13) and (14) are outlined and discussed.

### 3.3. Relationships between the characteristics of the macroscopic and microscopic descriptions

The plastic deformation described by Eq. (13) is basically controlled by two dislocation mechanisms: the multiplication and annihilation of dislocations characterized by the two parameters  $C_1$  and  $C_4$ , respectively. The flow stress increment produced by the plastic strain ( $\sigma_{p,cal}$ ) can be calculated using the well-known Taylor equation as:

$$\sigma_{p,cal} = \alpha \cdot \mu \cdot b \cdot (\sqrt{\rho} - \sqrt{\rho_0}), \quad (15)$$

where  $\alpha$  is a geometrical constant including the Taylor factor ( $\alpha = 0.7$  was selected for all fcc metals in these calculations),  $\mu$  is the shear modulus and  $b$  is the magnitude of the Burgers vector. Substituting the relationship for the dislocation density given in Eq. (14) into Eq. (15) gives:

$$\sigma_{p,cal} = \alpha \cdot \mu \cdot b \cdot \left\{ \sqrt{\frac{2C_1}{C_4} - \left(\frac{2C_1}{C_4} - \rho_0\right) \left(1 + \frac{C_4\varepsilon}{2}\right) \exp(-C_4\varepsilon)} - \sqrt{\rho_0} \right\}. \quad (16)$$

In addition to  $\alpha$ ,  $\mu$ ,  $b$  and  $\rho_0$ ,  $\sigma_{p,cal}$  depends also on the parameters  $C_1$  and  $C_4$  characterizing the microscopic processes of plastic deformation. Physically, the plasticity-induced flow stress increment in Eq. (16) can be correlated to the corresponding second term in the phenomenological Eq. (1):

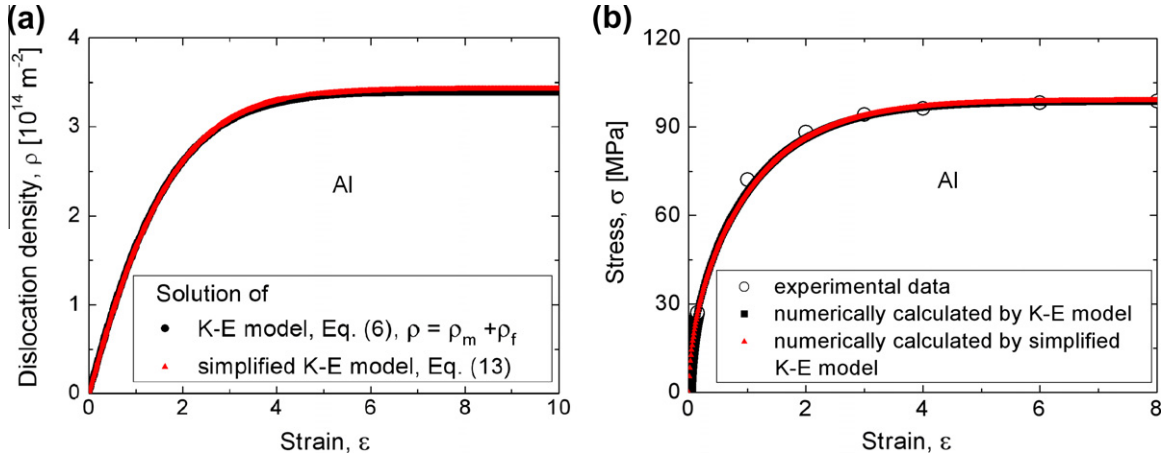


Fig. 4. The solution of Eqs. (6) and (13) for Al, showing (a) the evolution of the dislocation densities with strain and (b) the corresponding numerically calculated stress–strain curve together with the experimental data over a wide range of strain.

$$\sigma_{p,phen} = \sigma_1 \left\{ 1 - \exp \left[ - \left( \frac{\varepsilon}{\varepsilon_c} \right)^n \right] \right\}, \quad (17)$$

which is determined by the macroscopic parameters  $\sigma_1$ ,  $\varepsilon_c$  and  $n$ .

In order to study the possible correlations between the parameters of the microscopic and macroscopic descriptions of plastic behavior, it is necessary to examine the interdependence of Eqs. (16) and (17) in some special cases. First, making Eqs. (16) and (17) equal at high strains leads to:

$$\sigma_1 = \alpha \cdot \mu \cdot b \cdot \left( \sqrt{\frac{2C_1}{C_4}} - \sqrt{\rho_0} \right). \quad (18)$$

Furthermore, investigating the equality of Eqs. (16) and (17) at  $\varepsilon = \varepsilon_c$ , and neglecting  $\rho_0$  beside  $\frac{2C_1}{C_4}$  (as the value of  $\rho_0$  is 2–3 orders of magnitude lower than  $\frac{2C_1}{C_4}$ ), a value of the quantity  $C_4\varepsilon_c$  was obtained between 0.93 and 1.02 for these different fcc metals. It is reasonable to anticipate that  $C_4\varepsilon_c = 1$ , so that:

$$\varepsilon_c \approx \frac{1}{C_4}. \quad (19)$$

Fig. 5 shows the relationship between the quantities  $\frac{\sigma_1}{\alpha \cdot \mu \cdot b}$  and  $\sqrt{\frac{2C_1}{C_4}} - \sqrt{\rho_0}$  (Fig. 5a) as well as between the quantities  $\varepsilon_c$  and  $\frac{1}{C_4}$  (Fig. 5b) for different fcc metals, for which the value of  $\sigma_1$  and  $\varepsilon_c$ , and that of  $C_1$  and  $C_4$  are listed in Tables 1 and 3, respectively. The datum points in both figures are fitted well by straight lines which go through the origin. The slopes of  $\sim 1$  in Figs. 5a and 5b unambiguously confirm the validity of Eqs. (18) and (19) which describe the relationships between the characteristics ( $\sigma_1$ ,  $\varepsilon_c$ ) of the macroscopic description and ( $C_1$ ,  $C_4$ ) of the microscopic mechanisms. Eqs. (18) and (19) also mean that the values of  $C_1$  and  $C_4$  can be estimated from  $\sigma_1$  and  $\varepsilon_c$ .

In addition, making the derivatives of Eqs. (16) and (17) equal at  $\varepsilon = \varepsilon_c$  and using also the relationship  $C_4\varepsilon_c = 1$  leads to:

$$n = 0.75 \frac{\sqrt{\frac{2C_1}{C_4}}}{\sqrt{\frac{2C_1}{C_4}} - \sqrt{\rho_0}} = 0.78\text{--}0.85. \quad (20)$$

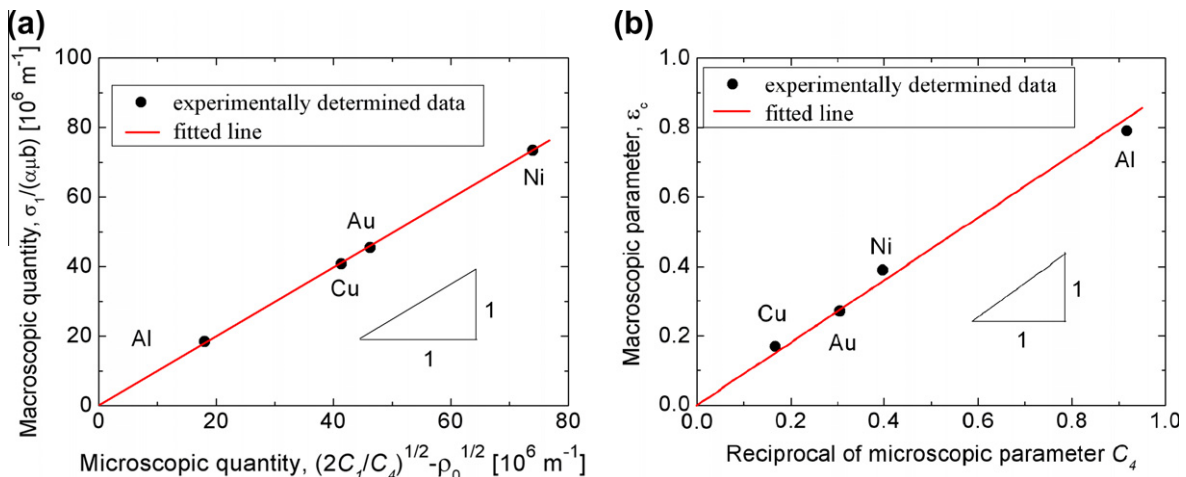


Fig. 5. The relationship between the characteristics of macroscopic and microscopic descriptions:  $\frac{\sigma_1}{\alpha \cdot \mu \cdot b}$  vs.  $\left( \sqrt{\frac{2C_1}{C_4}} - \sqrt{\rho_0} \right)$  (a), and  $\varepsilon_c$  vs.  $\frac{1}{C_4}$  (b) for different fcc metals.

Eq. (20) suggests that the macroscopic parameter  $n$  depends only slightly on  $C_1$  and  $C_4$  which indicates that, in practical terms, its value is not affected by any material-dependent feature of the multiplication and annihilation of dislocations. This calculated value of  $n$  is in good agreement with the values obtained from the fitting of the experimental data (see Table 1).

The results of the present analysis reveal that, while the saturation stress,  $\sigma_{sat}$ , is affected in a complex way by the microscopic processes of both dislocation formation and annihilation, the value of the macroscopic parameter,  $\varepsilon_c$ , depends only on the thermally activated dislocation trapping and annihilation mechanisms. The dependence of the saturation stress on the microscopic processes was discussed earlier [20]. Considering the significance of Eq. (19) in describing the relationship between the macroscopic parameter  $\varepsilon_c$  and the microscopic characteristic  $C_4$ , it can be seen that a higher value of  $C_4$  (and also  $C_2$ ) is associated with a smaller value of  $\varepsilon_c$ . On the other hand, and according to Eq. (17), at  $\varepsilon = \varepsilon_c$  the flow stress due to plastic deformation is  $\sigma_p = \sigma_1 \cdot [1 - \exp(-1)] \approx 0.63\sigma_1$ . Thus, the value of  $\varepsilon_c$  gives the strain where the plasticity-induced rise of the flow stress reaches  $\sim 63\%$  of the maximum increment characteristic for the saturation state. The larger values of the microscopic parameters,  $C_4$  and  $C_2$ , represent faster thermally activated trapping and annihilation of dislocations and thus lead to an earlier achievement of 63% of the maximum flow stress increment so that the macroscopic parameter,  $\varepsilon_c$ , is reduced.

#### 4. Summary and conclusions

- (1) Macroscopic and microscopic descriptions of the room temperature plastic behaviors of four representative fcc metals were investigated by analyzing the experimental stress–strain relationships and by simulations using theoretical modeling which incorporates the major micromechanisms of plastic deformation.
- (2) It is shown that over a wide range of strain the interaction between forest and mobile dislocations only marginally increases the forest density compared to the effect of the interaction between mobile dislocations.
- (3) The results of the simulations suggest that for the four fcc metals investigated (Al, Au, Cu, Ni), both the trapping of mobile dislocations and the annihilation of forest dislocations are controlled by the thermally activated non-conservative motion of dislocations. A simple model is suggested to interpret the similarity between these two dislocation-based micromechanisms.
- (4) Considering the same mechanism controls the trapping of mobile dislocations and the annihilation of forest dislocations, the applied theoretical model is simplified to give an analytical relationship for the evolution of the dislocation density as a function of strain.
- (5) Quantitative correlations are presented to demonstrate the primary features of the microscopic processes determining the parameters describing the macroscopic evolution of the stress–strain relationships during plastic deformation, thereby confirming the physical meaning of the macroscopic characteristics that are often used as fitting parameters.

#### Acknowledgements

This work was supported in part by the Hungarian Scientific Research Funds, OTKA, Grant No. K-81360 and K-67692 (N.Q.C. and J.G.) and in part by the National Science Foundation of the United States under Grant No. DMR-0855009 (T.G.L.). In addition, N.Q.C. thanks the Hungarian–American Enterprise Scholarship Fund for support. The European Union and the European Social Fund have provided financial support to this project under grant agreement no. TÁMOP 4.2.1./B-09/1/KMR-2010-0003.

#### References

- [1] Nabarro FRN, Basinski ZS, Holt DB. *Adv Phys* 1964;13:193.
- [2] Berner R, Kronmüller H. *Moderne probleme der metallphysik*. Berlin: Springer Verlag; 1965.
- [3] Kovacs I, Zsoldos L. *Dislocations and plastic deformation*. Budapest: Akademia Publisher; 1973.
- [4] Kocks UF, Mecking H. *Prog Mater Sci* 2003;48:171.
- [5] Zehetbauer M, Seumer V. *Acta Mater* 1993;41:577.
- [6] Zehetbauer M. *Acta Mater* 1993;41:589.
- [7] Valiev RZ, Islamgaliev RK, Alexandrov IV. *Prog Mater Sci* 2000;45:103.
- [8] Valiev RZ, Langdon TG. *Prog Mater Sci* 2006;51:881.
- [9] Zhilyaev AP, Langdon TG. *Prog Mater Sci* 2008;53:893.
- [10] Iwahashi Y, Horita Z, Nemoto M, Langdon TG. *Acta Mater* 1997;45:4733.
- [11] Iwahashi Y, Horita Z, Nemoto M, Langdon TG. *Acta Mater* 1998;46:3317.
- [12] Kocks UF. *J Eng Mater Technol* 1976;98:76.
- [13] Estrin Y, Mecking H. *Acta Metall* 1984;32:57.
- [14] Malygin GA. *Phys Status Solidi (a)* 1990;119:423.
- [15] Lukác P, Balík J. *Key Eng Mater* 1994;97(98):307.
- [16] Kubin LP, Estrin Y. *Acta Metall* 1990;38:697.
- [17] Estrin Y, Tóth LS, Molinari A, Brechet Y. *Acta Mater* 1998;46:5509.
- [18] Tóth LS, Molinari A, Estrin Y. *J Eng Mater Technol* 2002;124:71.
- [19] Chinh NQ, Horvath Gy, Horita Z, Langdon TG. *Acta Mater* 2004;52:3555.
- [20] Chinh NQ, Csanádi T, Gubicza J, Langdon TG. *Acta Mater* 2010;58:5015.
- [21] Hollomon JH. *Trans AIME* 1945;162:268.
- [22] Voce E. *J Inst Met* 1948;74:537.
- [23] Gubicza J, Kassem M, Ribárik G, Ungár T. *Mater Sci Eng A* 2004;372:115.
- [24] Fátay D, Bastarash E, Nyilas K, Dobatkin S, Gubicza J, Ungár T. *Z Metallk* 2003;94:842.
- [25] Schumacher S, Birringer R, Straus R, Gleiter H. *Acta Metall* 1989;37:2485.
- [26] Schafner E, Steiner G, Korznikova E, Kerber M, Zehetbauer MJ. *Mater Sci Eng A* 2005;410(411):169.